Chymotryptic specificity determinants in the 1.0 Å structure of the zinc-inhibited human tissue kallikrein 7

Mekdes Debela[†], Petra Hess[‡], Viktor Magdolen[§], Norman M. Schechter[¶], Thomas Steiner[‡], Robert Huber[‡‖††], Wolfram Bode[†], and Peter Goettig[†,††]

[†]Max-Planck-Institut für Biochemie, Proteinase Research Group, Am Klopferspitz 18, 82152 Martinsried, Germany; [‡]Max-Planck-Institut für Biochemie, Strukturforschung, Am Klopferspitz 18, 82152 Martinsried, Germany; [§]Klinische Forschergruppe der Frauenklinik der TU München, Ismaninger Strasse 22, 81675 Munich, Germany; [¶]Department of Dermatology, University of Pennsylvania, 415 Curie Boulevard, Philadelphia, PA 19104; and [‖]School of Biosciences, Cardiff University, Cardiff CF10 3TL, United Kingdom

Contributed by Robert Huber, August 18, 2007 (sent for review July 27, 2007)

hK7 or human stratum corneum chymotryptic enzyme belongs to the human tissue kallikrein (hKs) serine proteinase family and is strongly expressed in the upper layers of the epidermis. It participates in skin desquamation but is also implicated in diverse skin diseases and is a potential biomarker of ovarian cancer. We have solved x-ray structures of recombinant active hK7 at medium and atomic resolution in the presence of the inhibitors succinyl-Ala-Ala-Pro-Phe-chloromethyl ketone and Ala-Ala-Phe-chloromethyl ketone. The most distinguishing features of hK7 are the short 70–80 loop and the unique S1 pocket, which prefers P1 Tyr residues, as shown by kinetic data. Similar to several other kallikreins, the enzyme activity is inhibited by Zn^{2+} and Cu^{2+} at low micromolar concentrations. Biochemical analyses of the mutants H99A and H41F confirm that only the metal-binding site at His^{99} close to the catalytic triad accounts for the noncompetitive Zn^{2+} inhibition type. Additionally, hK7 exhibits large positively charged surface patches, representing putative exosites for prime side substrate recognition.

99 loop | desquamation | metal-binding proteinase | Netherlon syndrome

Human tissue kallikrein 7 (hK7), also called KLK7 or stratum corneum chymotryptic enzyme, is a member of the new human tissue kallikreins that lack the "kallikrein" insert of the 99 loop present in hK1–hK3. It is highly expressed in the upper spinous and granular layers of the epidermis (1) and was initially purified from human stratum corneum, the outermost layer of skin (2), where it plays a significant role in physiological and pathophysiological processes of the skin (3). hK7 is biosynthesized as an inactive precursor with a 22-aa signal peptide, followed by a 7-aa activation peptide and a 226-aa catalytic domain. After cleavage of the signal peptide, the proenzyme is activated *in vivo* by a still unknown extracellular protease with tryptic specificity, whereas *in vitro* hK5 or stratum corneum trypsin-like serine protease is able to activate pro-hK7 (4). The colocalization of hK5 and hK7 in human skin suggests a functional relationship (5, 6).

Because hK7 had been first identified in the skin, later studies focused mainly on its (patho-)physiological function in the epidermis. It was uncovered that hK7 and hK5 degrade intercellular cohesive structures in the stratum corneum, the so-called corneodesmosomes, a process that is required for shedding of cells at the skin surface, a prerequisite for the continuous regeneration of the skin (2–4, 7). Several protein components of the corneodesmosomes, such as desmoglein1, desmocollin1, and corneodesmosin, are good *in vitro* substrates of both hK7 and hK5 (4).

However, an elevated expression of hK7 in the epidermis leads to increased proteolytic activity, pathological desquamation, and inflammation in severe skin diseases such as Netherton syndrome, psoriasis, and atopic dermatitis (5, 7–10). Additionally, hK5 and hK7 exhibit several proinflammatory effects, including the activation of certain cytokines, the attraction of leukocytes, and the induction of proinflammatory activation cascades such as the kallikrein/kinin and complement systems (11).

Furthermore, hK7 may participate in multiple processes leading to invasive and metastatic tumor growth, especially in ovarian cancer. Whereas in healthy ovarian tissue, hK7 is produced at moderate concentrations, high levels of hK7 mRNA or protein were identified in ovarian cancers (11–15). The up to 15-fold hK7 overproduction correlates with ovarian cancer stage (16), and, moreover, a high level of hK7 mRNA is associated with a reduced overall survival of ovarian cancer patients (17). In line with these observations, overexpression of the *KLK4*, *5*, *6*, and *7* genes in a mouse tumor model increased the malignant phenotype of ovarian cancer cells (18). Thus, hK7 may contribute to metastasis by degrading extracellular matrix and adhesion molecules, enabling the tumor cells to disseminate from the primary tumor.

hK7 is one of the few human tissue kallikreins with well defined physiological and pathophysiological functions, and the first example of this family with chymotrypsin-like specificity to be crystallized as recombinant protein that we have purified from insect cells ($hK7_I$) and from *Escherichia coli* ($hK7_E$). The combined analysis of the hK7 structure and its substrate preference, which we have investigated in a specificity-profiling study (19), provides insights into the molecular determinants of the unique enzyme specificity and metal ion regulation.

Results and Discussion

Enzymatic Activity and Inhibition of hK7. Parameters of enzyme kinetics for recombinant $hK7_E$ were determined with fluorogenic substrates containing a single amino acid, to assess the distinct specificity of the S1 pocket. Both substrates exhibited a slow turnover at 25°C: for Phe-7-amino-4-methylcoumarin (Phe-AMC), values of $K_m = 44.3\ \mu M$, $k_{cat} = 0.000016\ s^{-1}$, and $k_{cat}/K_m = 0.36\ M^{-1}\ s^{-1}$ were obtained; and for Tyr-AMC, values of $K_m = 40.2\ \mu M$, $k_{cat} = 0.000033\ s^{-1}$, and $k_{cat}/K_m = 0.82\ M^{-1}\ s^{-1}$ were found. Thus, hK7 cleaves substrates with Tyr at P1 significantly faster, mainly because of an increased k_{cat} value. Even for the tetrapeptidic substrate succinyl (Suc)-Ala-Val-Pro-Phe(AVPF)-pNA a k_{cat}/K_m of only $16.0\ M^{-1}\ s^{-1}$ has been reported, indicating the requirement of extended substrate recognition for more efficient catalysis (20).

Author contributions: V.M., N.M.S., R.H., W.B., and P.G. designed research; M.D., P.H., N.M.S., T.S., and P.G. performed research; M.D., P.H., N.M.S., and P.G. analyzed data; and M.D., V.M., W.B., and P.G. wrote the paper.

The authors declare no conflict of interest.

Abbreviations: AMC, 7-amino-4-methylcoumarin; CMK, chloromethyl ketone; hK7, human tissue kallikrein 7; Suc, succinyl.

Data deposition: The atomic coordinates and structure factors have been deposited in the Protein Data Bank, www.pdb.org (PDB ID codes 2QXG, 2QXH, 2QXI, and 2QXJ).

[††]To whom correspondence may be addressed. E-mail: huber@biochem.mpg.de or goettig@biochem.mpg.de.

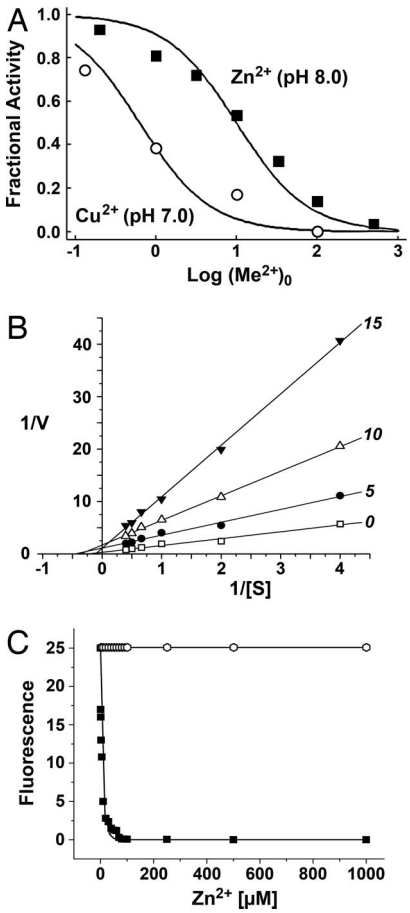

Fig. 1. Inhibition kinetics of hK7. (*A*) Inhibition curve of hK7 measured with the fluorogenic substrate Suc-AAPF-AMC and zinc and copper concentrations from 0.2 to 500 μM. The fractional activity is plotted against the logarithmic values of the metal ion concentration. (*B*) The Lineweaver–Burk plot for varying Suc-LLY-AMC concentrations and 0, 5, 10, and 15 μM Zn^{2+} demonstrates the noncompetitive inhibition type of hK7. (*C*) Activity of the hK7 mutants H41F (■) and H99A (open hexagons) against Suc-LLY-AMC with varying Zn^{2+} concentrations. The H99A mutation abolished the inhibitory effect of Zn^{2+} completely, whereas the H41F mutation caused no change with respect to the wild type.

Zinc and copper ions have a strong inhibitory effect on the hydrolytic activity of hK7, whereas calcium ions cause only a slight enhancement of the activity. For Zn^{2+}, an inhibition constant $K_{i(app)}$ of 10 μM was obtained with the substrate Suc-Ala-Ala-Pro-Phe(AAPF)-AMC, and, similarly, Cu^{2+} inhibited the enzymatic activity of hK7 at 0.6 μM (Fig. 1*A*). We conclude that the physiologically relevant Zn^{2+} ion plays a significant role in the regulation of the hK7 activity. A measurement series for 0, 5, 10, and 15 μM Zn^{2+} with Suc-Leu-Leu-Tyr(LLY)-AMC showed in a Lineweaver–Burk plot that the linear fits with increasing slopes intercept approximately at one point on the *x* axis, corroborating a noncompetitive inhibition for wild-type hK7 (Fig. 1*B*), similar to hK5 (21). Also, an Eadie–Hofstee plot of the same data confirmed this inhibition type. To distinguish between two potential inhibition sites, which were observed by crystallography, the activity of two hK7 mutants was analyzed for its Zn^{2+} dependence. Only H99A-hK7 exhibited virtually no Zn^{2+} inhibition, whereas the H41F mutant was inhibited as the wild type (Fig. 1*C*).

Overall Structure. Four hK7 crystal structures of identical polypeptide length containing two different peptidic inhibitors were solved. The $hK7_I$ structure in complex with a covalently bound Suc-AAPF-chloromethyl ketone (CMK) inhibitor was determined to 2.0 Å and 1.0 Å resolution, respectively. Also, a structure of this inhibitor complex with copper ions was solved at 2.1 Å. In contrast, refolded $hK7_E$ contains the covalently linked AAF-CMK and was refined to 2.6 Å (Table 1). These structures are rather similar, as reflected by the 0.4 Å rmsd of the Cα carbons, whereas significant deviations of the main chain only occurred in the surface loops between residues 36 and 38, and 70 and 80, according to the chymotrypsinogen numbering for tissue kallikreins (22), indicating an increased flexibility.

The hK7 molecule resembles an oblate ellipsoid with diameters of 35 and 50 Å (Fig. 2*A*). As in other chymotrypsin-like serine proteinases, the chain is folded into two six-stranded β-barrels and interconnected by three transdomain segments. The structure includes a 3_{10}-helix at segment Ala^{55}–Lys^{59} and two regular α-helices in segments Ser^{164}–Lys^{173} and Phe^{234}–Lys^{244}. The catalytic triad is located along the junction of both barrels, whereas the active-site cleft with the substrate recognition subsites S4 to S3′ runs perpendicular to this junction.

In mature hK7, the polypeptide chain starts with Ile^{16}, which forms via its α-ammonium group an internal salt bridge with the side-chain carboxylate of Asp^{194}. Formation of this salt bridge induces a functional active site as it stabilizes the oxyanion hole and a correctly shaped S1 pocket, which is accompanied by a rigidification of the activation domain (23, 24) (Fig. 2). Active hK7 terminates with Arg^{246} and exhibits the kallikrein-characteristic *cis*-Pro^{219} (22), as well as six intramolecular disulfide bridges. Noteworthy is the 70–80 loop of hK7 that is two residues shorter and more compact than in most other serine proteinases. The residues Ser and Ala at positions 70 and 80 preclude cation binding (see Fig. 2 *A* and *B*), whereas in pancreatic/coagulation proteinases both are often replaced by Glu residues, coordinating a stabilizing calcium ion (25).

Of particular interest are two large positively charged surface patches of hK7, which are reminiscent of the functionally important anion-binding exosites of thrombin (26) (Fig. 2*C*). The first of these two putative exosites, a surface depression to the right of the active-site cleft on the 70–80 loop (Fig. 2), consists of the basic residues Arg^{78}, Arg^{79}, Arg^{82}, and Arg^{113}, whereas the second exosite, extending along the C-terminal helix, comprises the basic residues Arg^{246}, His^{245}, Lys^{244}, Lys^{243}, Lys^{236}, Lys^{233}, and His^{91}, with the acidic Asp^{240} interspersed. Both positively charged regions nearly merge by several interjacent basic residues, such as Lys^{84}, Lys^{107}, Lys^{87}, Lys^{59}, and Arg^{90}, with only Glu^{62} providing a negative charge. Possibly, this large novel exosite binds negatively charged substrates or is bound to the cellular surface. Structural and functional modifications of this exosite may arise from the potential sugar linkage site ^{239}NDT, which was not glycosylated in $hK7_I$ expressed in insect cells.

Active-Site Cleft and Specificity. The residues of the catalytic triad, Ser^{195}, His^{57}, Asp^{102}, and the oxyanion hole, constituted by the main-chain amide nitrogens of Gly^{193} and Ser^{195}, are arranged in the active-site cleft of hK7 as in chymotrypsin (Fig. 2*B*). The S1 specificity pocket (27), which is bordered by the conserved segments Ala^{190}–Ser^{195}, Val^{213}–Cys^{220}, and Pro^{225}–Tyr^{228}, opens to the left of Ser^{195} and is larger than the S1 pockets of kallikreins hK1 (28) and hK4 (29) (Fig. 3 *A* and *B*). It resembles these kallikreins of trypsin-like specificity with the bulged-out 217–220 loop, with the Thr^{217} carbonyl directed toward the S1 pocket and the Phe^{218} carbonyl pointing away from it because of the following *cis*-Pro^{219}. However, the hK7 pocket differs from these kallikreins by the polar Asn^{189} at its bottom replacing the charged Asp^{189}, and by the Ser-replacing Ala^{190}, making the middle part of the pocket more hydrophobic. The entrance to this pocket is framed by the hydrophobic Phe^{218} and the polar Asn^{192} side chains, respectively. Thus, the S1 pocket with a polar bottom is wide but not as deep as that of chymotrypsin and is well suited for the accommodation of

BIOCHEMISTRY

Table 1. Data collection and refinement

Parameter	$hK7_E$	$hK7_I$	$hK7_I$–CU	$hK7_I$–HR
Space group $P2_1$, unit cell, Å	$a = 66.603$ $b = 42.708$ $c = 84.882$ $\alpha = \gamma = 90°, \beta = 108.53°$	$a = 38.301$ $b = 56.978$ $c = 45.560$ $\alpha = \gamma = 90°, \beta = 101.38°$	$a = 45.60$ $b = 41.155$ $c = 52.742$ $\alpha = \gamma = 90°, \beta = 92.53°$	$a = 38.254$ $b = 56.953$ $c = 45.533$ $\alpha = \gamma = 90°, \beta = 101.37°$
Resolution, Å	20.0–2.5	20.0–1.0	20.0–2.0	10.0–1.0
Unique reflections	14,065	96,121	12,308	97,071
Average multiplicity	2.7	2.9	3.3	3.3
R_{merge}, %	9.5 (33.3)	3.4 (31.6)	4.7 (26.3)	3.5 (28.0)
I/σ	15.4 (4.2)	27.4 (3.2)	25.0 (2.0)	9.7 (2.4)
Completeness, %	91.6 (89.0)	93.9 (84.9)	91.2 (59.3)	94.0 (89.6)
Resolution refinement, Å	20.0–2.6	20.0–2.0	20.0–2.1	10.0–1.0
Working set/Test set	11,955/642	11,740/624	10,539/568	92,134/4,932
R_{cryst}/R_{free}, %	26.6/29.2	18.0/23.3	21.7/25.1	13.1/15.9
Rmsd bond lengths, Å	0.004	0.006	0.006	0.015
Rmsd bond angles, °	1.221	1.511	1.394	0.336
Protein atoms [B factor, Å^2]	3,412 [26.1]	1,706 [13.4]	1,706 [38.4]	1,706 [13.8]
Inhibitor atoms	44 [23.7]	36 [20.5]	36 [46.5]	36 [13.7]
Solvent molecules/Cu^{2+} ions	228 [25.7]	167 [25.6]/2	86 [44.4] [66.0]	225 [25.8]
PDB ID code	2QXG	2QXH	2QXJ	2QXI

The statistic for $hK7_I$ includes two merged data sets for low and high resolution. Values in parentheses refer to the outermost shell of data collection, and brackets indicate B factors.

medium-sized to large side chains with polar tips, such as that of Tyr (Fig. 4). In contrast, unfavorable clashes would occur with Trp residues at the bottom of the pocket, as indicated by a superposition with the P1-Trp-containing bovine γ-chymotrypsin structure (30), in agreement with the low turnover of hK7 for P1 Trp substrates (19).

Both peptidic chloromethyl ketone inhibitors bind to the active-site cleft of hK7 in a canonical manner (Figs. 2*A* and 3 *A* and *B*),

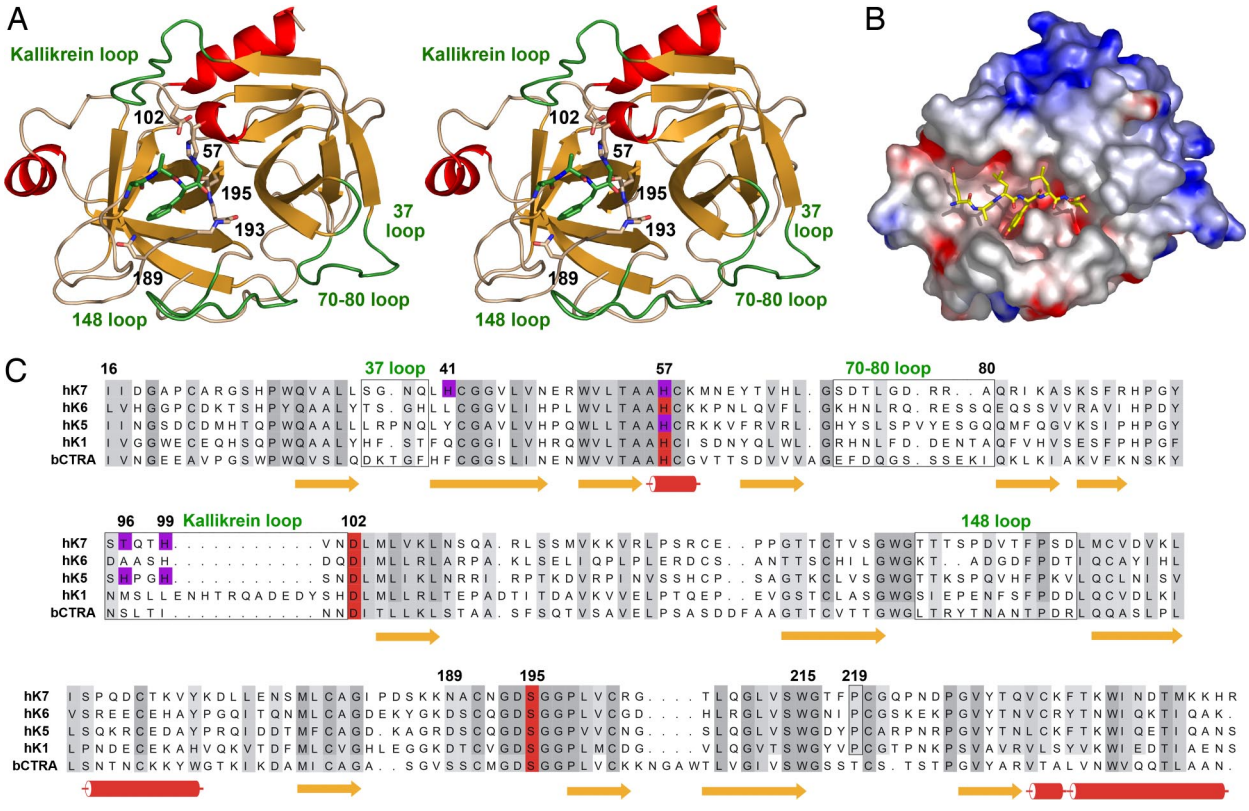

Fig. 2. Tertiary and primary structure of hK7. (*A*) Overall structure of $hK7_E$ monomer with the AAF-CMK inhibitor in a stereo ribbon representation. Side chains of the catalytic triad (His^{57}, Asp^{102}, Ser^{195}), the specificity-determining Asn^{189} in the S1 pocket, the oxyanion hole forming Gly^{193}, and the double covalently bound inhibitor are depicted as stick models. Important loops are labeled and highlighted in green. (*B*) Electrostatic surface representation for $hK7_I$ in a hypothetical complex with the modeled peptide Glu-Ala-Leu-Tyr-Leu-Val, occupying the specificity sites S4 to S2′. (*C*) Sequence alignment of hK7 with the tissue kallikreins hK6, hK1, hK5, and bovine chymotrypsin as a reference for numbering. Residues involved in metal binding are indicated by magenta background, whereas loops are surrounded by boxes.

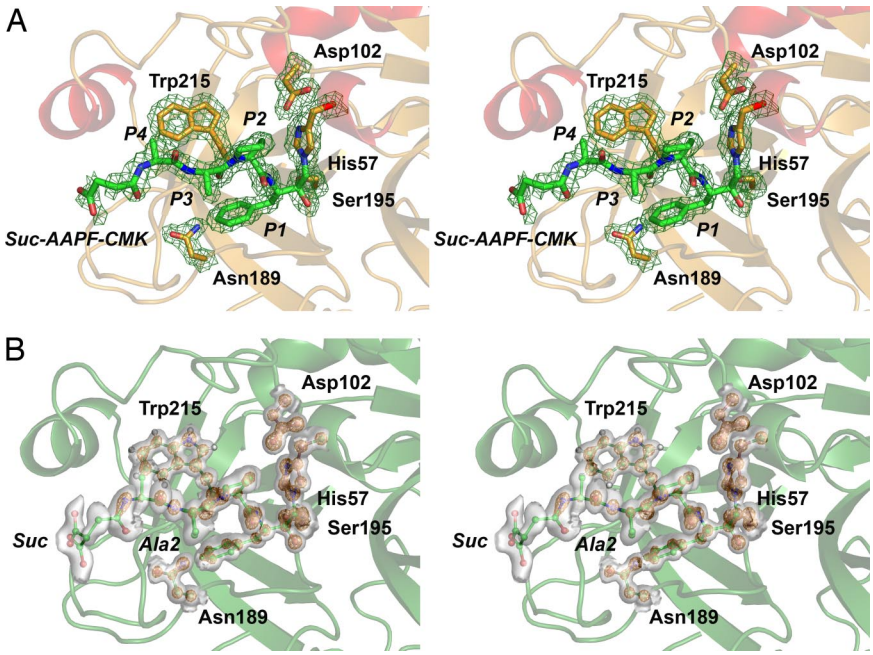

Fig. 3. Comparison of the hK7 active site at medium and atomic resolution. (*A*) Active site of hK7$_I$ with the Suc-AAPF-CMK inhibitor as stick model in stereo at 2.0 Å resolution with a $2F_o - F_c$ map contoured at 1.0σ. The inhibitor is covalently bound to the Nε of His^{57} and the Oγ of Ser^{195} and corresponds to substrate residues P4–P1. (*B*) The same view of the inhibitor at 1.0 Å resolution represented as a ball-and-stick model with a $2F_o - F_c$ map contoured at 1.0σ as transparent surface and contoured at 3.5σ as orange grid. Two alternative conformations with approximately equal occupancy are seen for the inhibitor Ala^2 side chain and the carboxylate of the succinyl group. In the Trp^{215} side chain, density for hydrogen atoms (white balls) is observed.

with their backbones juxtaposing segment Ser^{214}–Phe^{218} in an antiparallel manner, forming hydrogen bonds between P1-Phe N and Ser^{214} O, and between P3-Ala O/N and Gly^{216} N/O, besides the succinyl O and Phe^{218} N. The electron densities corroborate covalent bonds between Ser-195 Oγ and the P1-Phe carbonyl carbon as well as between His^{57} Nε2 and the methylene groups of both inhibitors. Both P1-Phe benzyl side chains extend partially into the S1 pocket between the peptide groups of Trp^{215}–Gly^{216} and Ala^{190}–Asn^{192} and are in van der Waals distance with the Val^{213} side chain and the Thr^{217} carbonyl oxygen. The cavity between the P1 phenyl ring, the Tyr^{228} phenol group, the Val^{213} side chain, and the Asn^{189} carboxamide group is occupied by three solvent molecules (Fig. 4). Both P2 side chains of Pro and Ala fit into the small hydrophobic niche bordered by the flat side of the His^{57} imidazolyl ring as well as by the His^{99} side chain. Both P3-Ala side chains extend away from the enzyme surface, whereas longer side chains could nestle to the side chains of Phe^{218} and Asn^{192}. Finally, the P4 side chain of the Suc-AAPF-CMK inhibitor points toward the triangular hydrophobic S4 cleft, which is based on the Trp^{215} indolyl side chain and bordered by the His^{99} imidazolyl and the Leu^{175} isobutyl side chains.

Details of the High-Resolution Structure. Although the 37 and 70–80 loops exhibit some disorder at 1.0 Å resolution, as seen in alternate atom positions both in the main chain (Leu^{74}, A74A) and several side chains, the relatively short kallikrein/99 loop seems to be quite rigid. The α-ammonium group of Ile^{16} is tightly bound by the carboxylate of Asp^{194} and the carbonyl O of Thr^{143}, whereas the following residues are more flexible, in particular, the main-chain atoms of Gly^{19} and Ala^{20} adopt distinct alternative conformations.

The benzyl side chain and the proline ring of the Suc-AAPF-CMK inhibitor are very well defined in the S1 and S2 pockets,

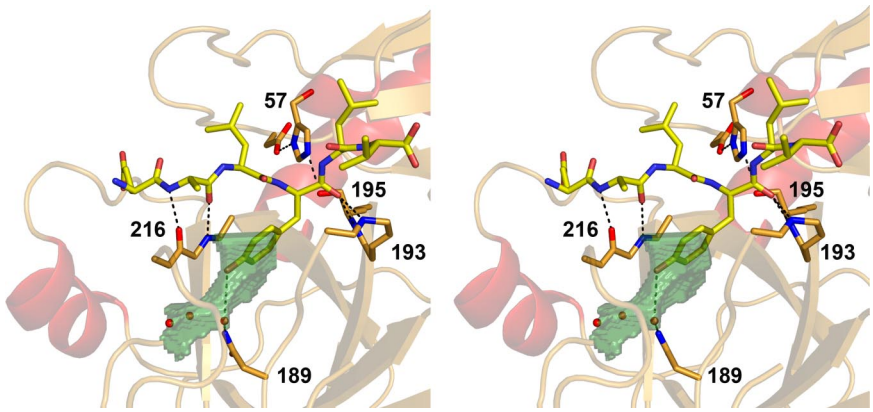

Fig. 4. Stick model of the modeled substrate Glu-Ala-Leu-Tyr-Leu-Val, the catalytic triad and the backbone of Gly^{193}, Ser^{195}, and Gly^{216} of hK7$_I$ in stereo, including hydrogen bonds as dotted lines. The S1 pocket is depicted as transparent green surface according to volume calculations with VOIDOO (41). The specificity for P1 Tyr is most likely conferred by Asn^{189} via hydrogen bonds from the carboxamide side chain to an interconnecting water molecule and to the Tyr OH group, respectively.

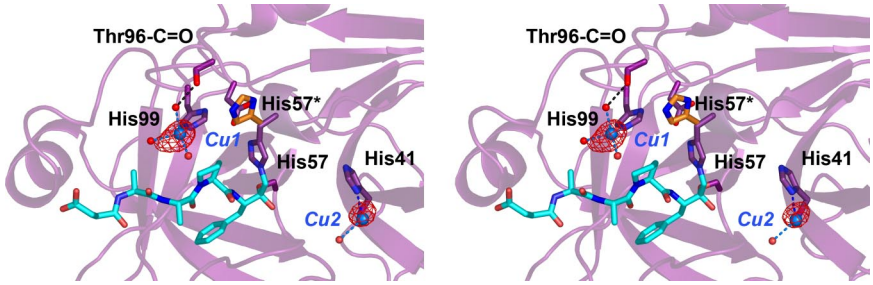

Fig. 5. The copper ions bound at His^{99} and His^{41} displayed as blue spheres surrounded by electron density of the anomalous Fourier map in red (contour 5σ) in stereo. His^{57} has the capacity for liganding Cu1 and Cu2 by a side chain rotation (His57*), requiring shifts of the ions, whereas the mutant H99A proves that only the His^{99} site is the structural basis for the Zn^{2+} and Cu^{2+} inhibition of hK7.

whereas two alternate conformations are observed for the main and side chain of Ala in P3 position, as well as two conformations of the succinyl carboxylate, which are rotated against each other by ≈60° (Fig. 3*B*). In the S1 pocket close to the carboxamide group of Asn^{189}, a water molecule is fixed by the Ala^{190} carbonyl O and by the amide of Gly^{221} in a position that allows for binding a hydroxyl group of a P1 Tyr. Most aromatic side chains exhibit only one rotational conformer as, e.g., Trp^{215}, which forms the hydrophobic floor of the S4 pocket and displays distinct electron density of the hydrogen atoms (Fig. 3*B*).

The Structural Basis of Zinc and Copper Ion Inhibition. Soaking with Zn^{2+} resulted in the destruction of hK7 inhibitor complex crystals, but a corresponding experiment with Cu^{2+} yielded crystals that diffracted to 2.0 Å resolution, although the cell constants changed significantly (Table 1). In the $2F_o - F_c$ electron density map, two peaks with strong density were identified and built in the model as Cu^{2+} ions. The first one (Cu1) is coordinated by the Nε2 of His^{99} via a water molecule by the main-chain carbonyl of Thr^{96}, and two additional water molecules, whereas the second (Cu2) appears to be only bound by the Nδ1 of His^{41} and a single water molecule. Both sites displayed peaks in an anomalous Fourier map, as expected for transition metal ions, but the one for Cu1 was much stronger (Fig. 5). Because Cu^{2+} and Zn^{2+} have nearly the same inhibitory effect on the activity of hK7, a dual interaction with His^{41} and His^{99} could be hypothesized, possibly by participation of His^{57} in the binding of the metal ions. However, the Zn^{2+} inhibition curve (Fig. 1*A*) and the noncompetitive character of the inhibition suggest a single inhibition site, which should be located to some extent apart from the substrate-binding site. These requirements would be met by the two metal sites described above. The mutational analysis (Fig. 1*C*) confirmed that only the His^{99} imidazole is the structural fundament of the Zn^{2+} inhibition. Nevertheless, the complete metal ion inhibition mechanism has still to be explained. On a structural level, the coordination of Zn^{2+} by His^{57}, His^{97}, and His^{99} in rat kallikrein 2 (31) represents the putative inhibited state of the proteinase, as it is assumed for hK5 (21). Intriguingly, the mutation R96H is sufficient for trypsin to be inhibited by Cu^{2+} and Zn^{2+} in the low micromolar range, and even more important, the metal ion is liganded by His^{96} and His^{57} that rotated out of the catalytic triad (32). Based on these striking parallels, we propose that the His^{57} of hK7 binds the inhibiting metal ions by a corresponding outward rotation, thereby disrupting and inactivating the catalytic triad.

Conclusion

Apparently, hK7 resembles more hK1, hK4, and hK6 than, for example, chymotrypsin, whereas its specificity can be classified as modified chymotrypsin-like with a unique P1 and P2 preference for Tyr (19). At S2, hK7 prefers Tyr over medium-sized hydrophobic and polar residues. Also, the S1 pocket of hK7 is more specific for Tyr than for Phe, Ala, or Met residues, which is mostly explained by the polar Asn^{189} at the bottom of the overall hydrophobic S1 pocket (Fig. 4).

The major Zn^{2+} inhibition site of hK7 has been unambiguously identified at His^{99} by the comparison of the H99A and H41F mutant inhibition kinetics. Despite the presence of only a second potential His ligand for Zn^{2+} (Fig. 5), the inhibition constant equals the one of hK5, which most likely binds the metal ion with the His^{57}, His^{96}, and His^{99} side chains (21). Probably, the strength of the Zn^{2+} coordination by the His^{96} Nδ1 is not much higher than the one by the Thr^{96} carbonyl via a water molecule. Nevertheless, for an optimal binding by the His^{57} Nε2, a shift of the Zn^{2+} with respect to the observed Cu^{2+} position is required. Because Zn^{2+} levels in the skin of mammals may nearly reach the millimolar range (33), this metal ion could be an important regulator of the hK7 activity, in addition to a recently described natural polypeptide inhibitor, lymphoepithelial Kazal-type related inhibitor (LEKTI). Intriguingly, hK7 has been found to colocalize with LEKTI in epidermal cells during desquamation (20), which might be of high physiological relevance (34).

Also, hK7 has been implicated in skin diseases and progression of ovarian and other cancer types. Thus, a better understanding of the hK7 enzymatic activity including the zinc inhibition based on our high-resolution structure could lead to the synthesis of selective small molecule inhibitors as antiinflammatory and potent anticancer therapeutics.

Materials and Methods

Purification of hK7. One form of recombinant hK7 was expressed in a baculovirus-insect cell system as a fusion protein with the segments ubiquitin, an enterokinase (EK) cleavage site, and mature hK7, as reported previously (20). Active $hK7_I$ was generated by removal of the ubiquitin tag with EK. Subsequently, $hK7_I$ was purified by affinity chromatography on a phenylbutylamine–Affi-Gel 10 resin followed by chromatography on heparin–Sepharose. The second recombinant form, $hK7_E$, was expressed in *E. coli* as inclusion bodies, refolded from urea, activated by cleavage of an artificial N terminus by EK, and purified as described previously (19). Mutagenesis was performed with mutated primers by PCR with *Pfu Turbo* (Stratagene, La Jolla, CA) and the original plasmid as template, which was afterward digested by DpnI (New England Biolabs, Ipswich, MA). The $hK7_E$ mutant proteins H41F and H99A were prepared according to protocol for the wild type.

Enzyme Kinetics. The hK7 activity was determined with the substrates Phe-AMC, Tyr-AMC, and Suc-LLY-AMC (Bachem, Bubendorf, Switzerland) ranging from 10 to 150 μM. Kinetic parameters of hK7 were determined in 50 mM Hepes, pH 7.5/150 mM NaCl/0.005% Tween 20 at 25°C from the initial velocity of the substrate cleavage at 221 nM concentration of hK7, whereas for the measurement series concerning the inhibition type 50 nM hK7 was used. The signal of the released AMC was fluorometrically recorded at excitation and emission wavelengths of 360 and 420 nm,

respectively. The fraction of active hK7 was measured by active-site titration with standardized bovine trypsin inhibitor as described previously (29) and Suc-LLY-AMC (Bachem) as substrate. Kinetic data were analyzed with Origin (OriginLab, Northampton, MA). The inhibition curve was measured at 25°C for an hK7 concentration of 100 nM with 85 μM Suc-AAPF-AMC in 100 mM Tris·HCl, pH 8.0/200 mM NaCl/9% DMSO with $CuCl_2$ and $ZnCl_2$ added in the range from 0.2 to 200 and 500 μM, respectively (excitation at 370 nm and emission at 475 nm). For calculation of the inhibition constant $K_{i(app)}$ the following formula was used:

$$FA = 1/(10(\log[\mathrm{Me}]_0 - \log K_{i(app)}) + 1) \quad [1]$$

where FA denotes the fractional activity (V/V_0) of the enzyme obtained for the various metal ion (Me) concentrations.

Crystallization, Data Collection, and Refinement. The two recombinant hK7 species, complexed with the inhibitors AAF-CMK and Suc-AAPF-CMK, yielded different crystal forms at 18°C by the sitting-drop vapor diffusion method. Crystal form 1 grew in drops of 1 μl of protein solution (7 mg/ml $hK7_E$-AAF-CMK complex) and 1 μl of 100 mM [bis(2-hydroxyethyl)amino]tris(hydroxymethyl)-methane·HCl, pH 6.0/ 25% PEG 3350/2.5 M Li_2SO_4, equilibrated against 500 μl of reservoir buffer. These crystals were mounted under a nitrogen gas stream at 100 K and diffracted beyond 2.0 Å resolution at the synchrotron (beamline BW6; DESY, Hamburg, Germany). They belong to the monoclinic space group $P2_1$ and contain two monomers per asymmetric unit (see Table 1). The crystals of the $hK7_I$-Suc-AAPF-CMK complex were grown from 2.5 μl of protein solution and 1.5 μl of 100 mM sodium cacodylate, pH 6.5/200 mM magnesium acetate/30% (vol/vol) 2-methyl-2,4-pentanediol with 500 μl of reservoir buffer. The $hK7_I$-Suc-AAPF-CMK crystals were transferred to crystallization buffer with 20% glycerol and diffracted beyond 1.0 Å resolution (BW6). Two datasets for low- and high-resolution data were collected. These crystals belonged to the space group $P2_1$ with one molecule per asymmetric unit, but they changed their cell constants significantly upon soaking with 10 mM $CuSO_4$ solution (Table 1).

These data were evaluated with MOSFLM (42) and scaled with SCALA (www.ccp4.ac.uk/ccp4Lmain.php) and DENZO/SCALEPACK (35), respectively. Molecular replacement searches were performed with PHASER (36) by using the coordinates of hK6 [Protein Data Bank (PDB) ID code 1LO6]. In the case of $hK7_E$-AAF-CMK, the best solution had a log-likelihood gain (LLG) of +266 and Z values for the rotation function (RFZ) of 7.3 and of 15.4 for the translation function (TFZ), whereas the best solution for $hK7_I$-AAPF-CMK reached a LLG of +147 with Z values of RFZ = 8.1 and TFZ = 7.1. For $hK7_I$-Suc-AAPF-CMK-Cu using the refined $hK7_I$-Suc-AAPF-CMK model, PHASER found a solution with a LLG of +1,617 and Z values of RFZ = 34.2 and TFZ = 34.1.

The correctness of the replacement solutions was validated by inspecting the packing of symmetry-related molecules and with composite omit maps calculated in CNS (43). Model building for $hK7_E$-AAF-CMK was performed with the program O and refinement with CNS, resulting in final R_{cryst} and R_{free} values of 26.6% and 29.2%, respectively, for a maximum resolution of 2.6 Å (Table 1). Several cycles of refinement in CNS and model building for $hK7_I$-Suc-AAPF-CMK with MAIN (44) and CNS, using standard target values (37), resulted in final R_{cryst} and R_{free} of 18.0% and 23.3% for data to 2.0 Å (Table 1). The whole main chain of the hK7 catalytic domain is well defined by electron density, except for a few side chains whose occupancy was set at zero. The copper-containing $hK7_I$-Suc-AAPF-CMK-CU model was refined to R_{cryst} and R_{free} of 21.7% and 25.1%, respectively, at 2.1 Å resolution.

For the high-resolution structure of $hK7_I$-Suc-AAPF-CMK, the refined 2.0 Å model was used for rigid body and conjugate gradient refinement with SHELX-97 (http://shelx.uni-ac.gwdg.de/) to 1.5 Å. Alternate conformations were built including multiple positions of water molecules with XTALVIEW (www.sdsc.edu/CCMS/Packages/XTALVIEW/xtalview.html) and COOT (38). Subsequently, anisotropic B factors and occupancies of alternate atom positions were refined to 1.0 Å resolution. In the final refinement cycles, the riding hydrogen model was used, resulting in R_{cryst} of 13.1% and an R_{free} of 15.9%. All figures were created with PMOL version 0.98 (39), whereas the potential phi map was calculated with GRASP (40).

We are thankful to R. Faessler for support of this work and to G. Bourenkov and G. Kalachova for help with data collection. We are grateful to Zhi-Mei Wang and Eun-Jung Choi for the preparation of recombinant $hK7_I$. This work was supported by the European Commission (CAMP; LSHG-2006–018830), by the Fonds der Chemischen Industrie (to W.B.), by the Kommission Klinische Forschung der TU München (to V.M.), and by the Graduiertenkolleg 333 der Deutschen Forschungsgemeinschaft (to M.D.).

1. Egelrud T, Hofer PA, Lundstrom A (1988) *Acta Derm Venereol* 68:93–97.
2. Egelrud T (1993) *J Invest Dermatol* 101:200–204.
3. Egelrud T, Lundstrom A (1991) *Arch Dermatol Res* 283:108–112.
4. Caubet C, Jonca N, Brattsand M, Guerrin M, Bernard D, Schmidt R, Egelrud T, Simon M, Serre G (2004) *J Invest Dermatol* 122:1235–1244.
5. Egelrud T, Brattsand M, Kreutzmann P, Walden M, Vitzithum K, Marx UC, Forssmann WG, Magert HJ (2005) *Br J Dermatol* 153:1200–1203.
6. Brattsand M, Stefansson K, Lundh C, Haasum Y, Egelrud T (2005) *J Invest Dermatol* 124:198–203.
7. Ekholm E, Egelrud T (1999) *Arch Dermatol Res* 291:195–200.
8. Hansson L, Backman A, Ny A, Edlund M, Ekholm E, Ekstrand Hammarstrom B, Tornell J, Wallbrandt P, Wennbo H, Egelrud T (2002) *J Invest Dermatol* 118:444–449.
9. Johnson B, Horn T, Sander C, Kohler S, Smoller BR (2003) *J Cutan Pathol* 30:358–362.
10. Ny A, Egelrud T (2003) *Acta Derm Venereol* 83:322–327.
11. Wang X, Wang E, Kavanagh JJ, Freedman RS (2005) *J Transl Med* 3:25.
12. Shigemasa K, Tanimoto H, Underwood LJ, Parmley TH, Arihiro K, Ohama K, O'Brien TJ (2001) *Int J Gynecol Cancer* 11:454–461.
13. Bondurant KL, Crew MD, Santin AD, O'Brien TJ, Cannon MJ (2005) *Clin Cancer Res* 11:3446–3454.
14. Dong Y, Kaushal A, Brattsand M, Nicklin J, Clements JA (2003) *Clin Cancer Res* 9:1710–1720.
15. Tanimoto H, Underwood LJ, Shigemasa K, Yan Yan MS, Clarke J, Parmley TH, O'Brien TJ (1999) *Cancer* 86:2074–2082.
16. Shan SJ, Scorilas A, Katsaros D, Rigault de la Longrais IA, Massobrio M, Diamandis EP (2006) *Clin Chem* 52:1879–1886.
17. Kyriakopoulou LG, Yousef GM, Scorilas A, Katsaros D, Massobrio M, Fracchioli S, Diamandis EP (2003) *Clin Biochem* 36:135–143.
18. Prezas P, Arlt MJ, Viktorov P, Soosaipillai A, Holzscheiter L, Schmitt M, Talieri M, Diamandis EP, Kruger A, Magdolen V (2006) *Biol Chem* 387:807–811.
19. Debela M, Magdolen V, Schechter N, Valachova M, Lottspeich F, Craik CS, Choe Y, Bode W, Goettig P (2006) *J Biol Chem* 281:25678–25688.
20. Schechter NM, Choi EJ, Wang ZM, Hanakawa Y, Stanley JR, Kang Y, Clayman GL, Jayakumar A (2005) *Biol Chem* 386:1173–1184.
21. Debela M, Goettig P, Magdolen V, Huber R, Schechter N, Bode W (2007) *J Mol Biol*, in press.
22. Bode W, Chen Z, Bartels K, Kutzbach C, Schmidt-Kastner G, Bartunik H (1983) *J Mol Biol* 164:237–282.
23. Bode W, Schwager P, Huber R (1978) *J Mol Biol* 118:99–112.
24. Huber R, Bode W (1978) *Acc Chem Res* 11:114–122.
25. Bode W, Schwager P (1975) *FEBS Lett* 56:139–143.
26. Bode W, Turk D, Karshikov A (1992) *Protein Sci* 1:426–471.
27. Schechter I, Berger A (1967) *Biochem Biophys Res Commun* 27:157–162.
28. Laxmikanthan G, Blaber SI, Bernett MJ, Scarisbrick IA, Juliano MA, Blaber M (2005) *Proteins* 58:802–814.
29. Debela M, Magdolen V, Grimminger V, Sommerhoff C, Messerschmidt A, Huber R, Friedrich R, Bode W, Goettig P (2006) *J Mol Biol* 362:1094–1107.
30. Harel M, Su CT, Frolow F, Silman I, Sussman JL (1991) *Biochemistry* 30:5217–5225.
31. Fujinaga M, James MN (1987) *J Mol Biol* 195:373–396.
32. McGrath ME, Haymore BL, Summers NL, Craik CS, Fletterick RJ (1993) *Biochemistry* 32:1914–1919.
33. Nitzan YB, Sekler I, Silverman WF (2004) *J Histochem Cytochem* 52:529–539.
34. Descargues P, Deraison C, Bonnart C, Kreft M, Kishibe M, Ishida-Yamamoto A, Elias P, Barrandon Y, Zambruno G, Sonnenberg A, Hovnanian A (2005) *Nat Genet* 37:56–65.
35. Otwinowski Z, Minor W (1997) *Methods Enzymol* 276:307–326.
36. McCoy AJ, Grosse-Kunstleve RW, Storoni LC, Read RJ (2005) *Acta Crystallogr D* 61:458–464.
37. Engh RA, Huber R (1991) *Acta Crystallogr A* 47:392–400.
38. Emsley P, Cowtan K (2004) *Acta Crystallogr D* 60:2126–2132.
39. DeLano WL (2002) (DeLano Scientific, San Carlos, CA).
40. Nicholls AR, Sharp K, Honig B (1991) *Proteins* 11:281–296.
41. Kleywegt GJ, Jones TA (1994) *Acta Crystallogr D* 50:178–185.
42. Leslie AGW (1992) *Int CCP4/ESF-EACMB Newslett Protein Crystallogr* 26.
43. Brunger AT, Adams PD, Clore GM, Gros P, Grosse-Kunstieve RW, Jiang JS, Kuszewsji J, Nilges M, Pannu NS, *et al*. (1988) *Acta Crystallogr D* 54:905–921.
44. Turk D (1992) PhD thesis (Techische Universität München, Munich).